Check for updates

ASME Journal of Solar Energy Engineering
Online journal at:
https://asmedigitalcollection.asme.org/solarenergyengineering

Julian J. Krauth
DLR (German Aerospace Center),
Institute of Solar Research,
Calle Doctor Carracido 44,
Almería 04005, Spain
e-mail: julian.krauth@dlr.de

Christoph Happich
CSP Services,
Friedrich-Ebert-Ufer 30,
51143 Cologne, Germany
e-mail: c.happich@cspservices.de

Niels Algner
DLR (German Aerospace Center),
Institute of Solar Research,
Calle Doctor Carracido 44,
Almería 04005, Spain
e-mail: niels.algner@dlr.de

Rafal Broda[1]
DLR (German Aerospace Center),
Institute of Solar Research,
Calle Doctor Carracido 44,
Almería 04005, Spain
e-mail: rafal.broda@dlr.de

Andreas Kämpgen
CSP Services,
Paseo de Almería 73,
Almería 04001, Spain
e-mail: a.kaempgen@cspservices.de

Alexander Schnerring
DLR (German Aerospace Center),
Institute of Solar Research,
Calle Doctor Carracido 44,
Almería 04005, Spain
e-mail: alexander.schnerring@dlr.de

Steffen Ulmer
CSP Services,
Paseo de Almería 73,
Almería 04001, Spain
e-mail: s.ulmer@cspservices.de

Marc Röger
DLR (German Aerospace Center),
Institute of Solar Research,
Calle Doctor Carracido 44,
Almería 04005, Spain
e-mail: marc.roeger@dlr.de

HelioPoint – A Fast Airborne Calibration Method for Heliostat Fields

The pointing calibration of a newly built heliostat field can take up to several years. The state-of-the-art method typically used is accurate but slow. A faster method could reduce the commissioning time and therefore increase the viability of a solar tower plant significantly. In this work, we present HelioPoint, a fast airborne heliostat calibration technique, and demonstrate its accuracy to be better than 0.3 mrad. The measurement is performed using a light-emitting diode (LED) and a camera fitted to a drone. The only infrastructure required is the roughly pre-aligned heliostats themselves. The method is independent of the sun position and can be performed at any time for arbitrary calibration points.
[DOI: 10.1115/1.4065868]

Keywords: heliostat, calibration, drone, unmanned aerial vehicle, airborne, deflectometry, reflectometry, led, pointing, offset, optimization, concentrating solar power, renewable, solar field, tracking, solar tower, measurement, optics

Introduction

Heliostats are an integral part of solar tower plants. They consist of one or more mirror facets arranged in a way to concentrate solar radiation at a given distance. To focus the sunlight onto a central

[1]Corresponding author.
Contributed by the Solar Energy Division of ASME for publication in the Journal of Solar Energy Engineering: Including Wind Energy and Building Energy Conservation. Manuscript received December 20, 2023; final manuscript received April 12, 2024; published online July 19, 2024. Assoc. Editor: Guangdong Zhu.

Copyright © 2024 by ASME; reuse license CC-BY 4.0

Downloaded from http://asmedigitalcollection.asme.org/solarenergyengineering/article-pdf/146/6/061005/7354605/sol_146_6_061005.pdf by DLR Deutsches Zentrum F Luft-U Raumfahrt Ev user on 04 November 2024

receiver, the heliostats track the angle bisector between the "moving" sun incident vector and the vector pointing from the heliostat to the receiver. The orientation needs to be updated every few seconds. However, inaccuracies in construction as well as sensor and actuator errors lead to tracking errors, i.e., deviations from the desired optical axis of the heliostat, with a strong impact on solar field performance. Calibrating the heliostats allows the operator to correct such errors, reducing the spillage losses and ensuring a well-controlled irradiance distribution on the receiver.

The parameters to precisely describe the heliostat movement with a kinematic model can be determined only if several orientations of a heliostat are measured, creating an overdetermined parameter system. The different orientations used for calibration are called calibration points. A heliostat counts as fully calibrated (calibration is valid for arbitrary positions) if all degrees of freedom can be determined precisely. Depending on the heliostat, this results in about 10–30 calibration points to be measured, covering the full heliostat movement over the course of the year.

The required pointing accuracy depends on the dimensions of the solar tower plant. However, as a general rule of thumb, in large commercial plants, the heliostat orientation should be known and controlled on a smaller-equal 1-mrad level.[2] For a new solar tower plant, the heliostats are first roughly aligned during construction. Afterwards, a fine calibration with an accuracy of ≤ 0.3 mrad is needed for each calibration point [1]. The current state-of-the-art method for a fine calibration is a one-by-one calibration procedure, also known as a camera-target method, in which the sunlight is reflected by a heliostat onto a white diffusive reflective target plane attached to the central tower. A camera takes pictures of the target and from the centroid position of the reflected light spot the heliostat orientation is determined [2]. This method has three major drawbacks.

First, the measurement is dependent on the sun. A specific orientation can only be calibrated during a specific sun position, i.e., for a specific time of day and year, during sunlight. Furthermore, the sun shape and appearance influence the measurement.

Second, a heliostat field of a solar tower plant can consist of over a hundred thousand heliostats. A sequential calibration method like the camera-target method is very slow and can take up to several years for the complete calibration of an entire solar field.

Third, the tower and target must be available (i.e., its construction must be completed and safe to calibrate on).

The HelioCon roadmap [3] therefore identifies the improvement of the calibration procedure as a crucial step toward increased cost efficiency.

Although several other heliostat calibration and tracking control methods exist or have been proposed [1], no faster and still equally precise method has yet gained market acceptance. Building on our earlier work [4,5], we now present a fast airborne calibration method for heliostats and demonstrate its competitive accuracy. The method determines the actual orientation of the heliostat optical axis.[3] It can be applied non-intrusively to larger groups of heliostats at once, independent of the time of day and year, significantly accelerating the calibration procedure. Furthermore, it does not rely on any other infrastructure compared to other promising methods [6]. The simple and fast procedure also increases the feasibility of performing a second calibration a couple of years after commissioning and has the potential to be further developed into an O&M tool.

Methods

The HelioPoint method takes advantage of the law of reflection to determine the heliostat orientation using a strong light-emitting diode (LED) and a camera fitted to a drone (see Fig. 1, left). Both LED and camera are pointed toward the heliostats to be calibrated. Calibration in the case of HelioPoint means that we assume a *fixed* kinematic model, i.e., all parameters describing the kinematic model of the heliostat are assumed to be correct as provided by the operator. Accordingly, only the tracking angles are calibrated. If the drone is positioned near the optical axis of a heliostat, a reflection of its LED can be detected in the image (see Fig. 1, right). The orientation of the heliostat surface at the detected reflection point is then determined by means of the known heliostat position as well as the drone position, i.e., the position of camera and LED.

Even though the calibration procedure can be performed on one individual heliostat, it is typically applied to clusters of several heliostats pointing at a defined camera position. This allows to obtain data on several heliostats from one single image as shown in Fig. 2. To account for surface and tracking errors, it is necessary to collect multiple sampling points from different drone positions by flying along a predefined pattern. This pattern preferably lies in a plane approximately perpendicular to the optical axes of the measured heliostats. The pattern should be defined in such a way that the sampling points are homogeneously distributed over the entire heliostat aperture area, covering all facets. In addition, depending on the heliostat geometry and the quality of the mirror shape, a certain minimum number of sampling points per heliostat should be achieved, which can be determined empirically or from simulations.

The complete measurement procedure from flight route planning to data analysis involves several steps which are explained below. Since the method was tested at the DLR solar tower test facility in Jülich, Germany, some of the following figures exemplarily show its heliostat field. However, the procedure is prepared to cover large industry-sized power plants.

Calibration Points and Grouping Heliostats. Typically, the operator of a power plant uses a set of specific orientations for each heliostat that are calibrated against a reference to ensure a given pointing accuracy for general tracking angles during operation. The orientations in this set are called calibration points. The number of calibration points needs to be larger than the degrees of freedom in the kinematic model of the heliostat, including not only design parameters such as the tracking angles azimuth and elevation, but also parameters such as the imprecise installation of the foundation, the pylon, etc. These calibration points are the same orientations that need to be measured by the method presented here. For that, the solar field is divided into sections of equal area yielding multiple clusters of heliostats. The number of heliostats per cluster varies with the heliostat density depending on the heliostat size and the location within the solar field. Each cluster is calibrated for the same calibration points, i.e., all heliostats in one cluster point to one camera position. This results in a slightly different orientation for each heliostat within a cluster. A threshold for this variation is defined, setting the maximum area size of the clusters for a given camera distance. The cluster area has a roundish shape of typically about 100 m in diameter.

Flight Route Planning and Data Acquisition. For each heliostat cluster and each calibration point, camera and LED fitted to a drone move along a defined pattern on a plane roughly perpendicular to the heliostat orientations at a distance of up to several hundred meters from the heliostat cluster, depending on various, mostly geometric and technical, constraints. The size of the flight pattern is derived from the expected heliostat pointing accuracy and the distance to the heliostats. While the drone is moving along this pattern an image series is recorded. In these images, the LED should be seen reflected by those heliostats where the drone is close to the optical axis. After the drone has finished the flight pattern, it moves on to cover a calibration point of the next cluster. Then, a new image series is recorded during the next flight pattern for the second cluster, and so on. While the drone

[2]Large plants can reach heliostat-to-tower distances of more than 1 km; assuming a distance of 1 km and a tracking error of 1 mrad, an offset of around 2 m between the desired and the target aim point would be observed.

[3]We define the optical axis as the mean axis of all normal vectors of the entire mirror surface of a heliostat.

Downloaded from http://asmedigitalcollection.asme.org/solarenergyengineering/article-pdf/146/6/061005/7354605/sol_146_6_061005.pdf by DLR Deutsches Zentrum F Luft-U Raumfahrt Ev user on 04 November 2024

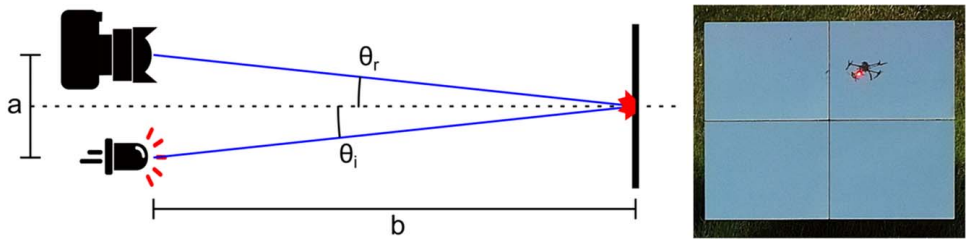

Fig. 1 Left: calibration principle not to scale. LED and camera (left) have a fixed distance (*a*) of a few centimeters to each other and are fitted to a drone (not shown). The drone has a distance (*b*) to a mirror surface (right) of up to few 100 m. If a reflection can be seen in the camera image, the normal (dashed line) of that specific part of the mirror surface is the bisector $(\theta_i + \theta_r)/2$ between LED and camera. Right: section of a recorded image showing the reflected drone and LED on a heliostat.

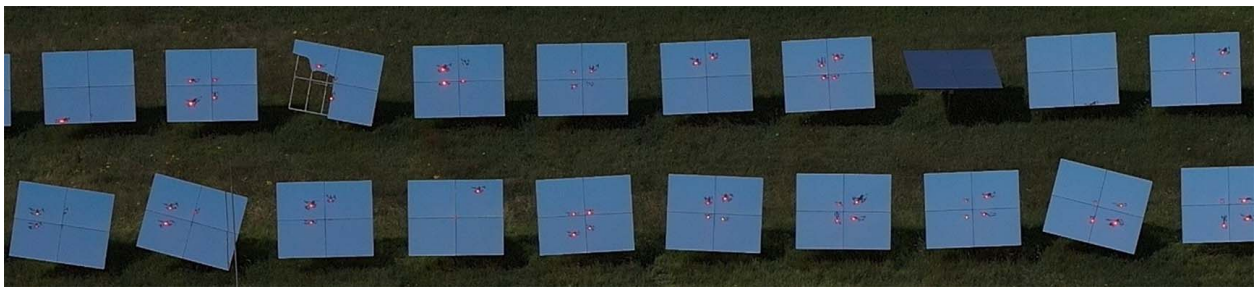

Fig. 2 Heliostats at the DLR solar tower test facility in Jülich, Germany. All heliostats with LED reflections are pointing closely toward a single drone carrying an LED and a camera.

measures a calibration point in one cluster, the heliostats in another cluster can be adjusted. In this way, all the clusters and calibration points can be measured successively. If more drones are used, the data acquisition can also be parallelized.

Data Analysis. Each LED reflection detected in an image can be used to derive the normal vector of the corresponding mirror at the specific location of the reflection. For the determination of the precise direction of that normal vector, the positions of heliostat, camera, and LED have to be known. Typically, the heliostat positions can be provided by the operator of the plant with sufficiently high accuracy. If not, one can for example perform a photogrammetric measurement to obtain the heliostat positions. The initial task is to identify which heliostat identification (ID) corresponds to which heliostat in the image. Using an image processing algorithm based on classical computer vision methods, all the heliostats and their mirror corners on the images can be detected. By means of a real-time kinematics (RTK) capable drone, the offset-corrected global positioning system (GPS) positions (accuracy about 10 mm, see Appendix A) of the drone, as well as the camera gimbal angles for each image, are obtained. Using a calibrated camera model, the heliostat positions can be projected onto the image allowing the identification of the individual heliostats. In case the projection is not accurate enough for unambiguous identification, the external camera orientation of the camera can be improved – depending on the gimbal stability – using automatic or manual feature matching.

In the next step, again using an image processing algorithm, the LED reflections on each heliostat are detected and the positions of the centroids of the reflections are transformed from image coordinates into the concentrator coordinate system (CCS) of the respective heliostat. Note that due to facet canting and shape deviations of real heliostats, several reflections of the LED may appear on the heliostat surface in the same image. The data can be treated in the same way contributing to the statistics.

For each heliostat, the reflections from all images are collected. In the first iteration, their *measured* normal vectors $\boldsymbol{n}_{\text{meas}}$ are calculated using the corresponding camera position and the *expected* heliostat orientation (see Fig. 3) by

$$\boldsymbol{p}_{\text{reflex}} = \boldsymbol{p}_{\text{helio}} + \mathbf{K}_{\text{helio}}\,(k_1, k_2, \ldots; \varphi_1, \varphi_2; x_{\text{CCS}}, y_{\text{CCS}}) \tag{1}$$

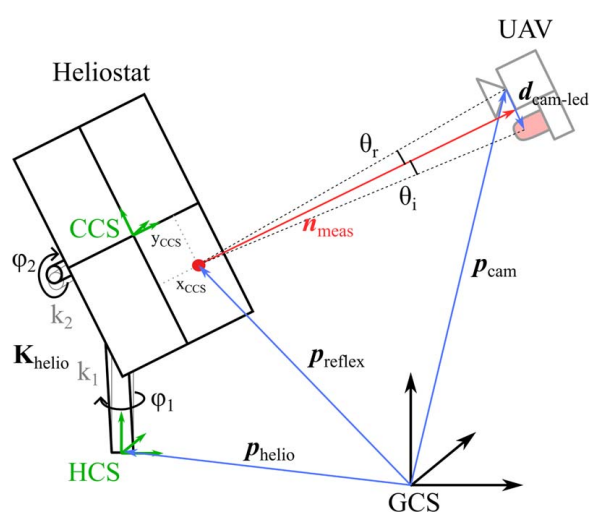

Fig. 3 Sketch indicating the relevant vectors and geometries for calculating the normal vector corresponding to a reflection of the LED seen by the camera. The sketch is not to scale. The heliostat geometry and tracking axes shown here are meant to represent a generic model that can be different from the one shown. $\mathbf{K}_{\text{helio}}$ is the kinematic model of a heliostat parametrized with $k_1, k_2, \ldots$ and tracking angles φ_1 and φ_2. CCS and HCS denote the coordinate systems of concentrator and heliostat, respectively. The *p* vectors indicate the position of the corresponding objects with respect to a GCS. *d* is the vector pointing from the principle point of the camera to the center of the LED. The measured normal vector n_{meas} is the bisector between incident θ_i and reflected θ_r lines.

Downloaded from http://asmedigitalcollection.asme.org/solarenergyengineering/article-pdf/146/6/061005/7354605/sol_146_6_061005.pdf by DLR Deutsches Zentrum F Luft-U Raumfahrt Ev user on 04 November 2024

$$\boldsymbol{n}_{\text{meas}} = \boldsymbol{p}_{\text{cam}} + \boldsymbol{d}_{\text{cam-led}}\,(\text{pitch, yaw})/2 - \boldsymbol{p}_{\text{reflex}} \tag{2}$$

where the $\boldsymbol{p}$ vectors indicate the position of reflection, heliostat, and camera, respectively, $\mathbf{K}_{\text{helio}}$ is the kinematic model with parameters k_i and the assumed tracking angles φ_1, φ_2, which converts the reflex position $(x_{\text{CCS}}, y_{\text{CCS}})$ given in CCS into the heliostat coordinate system (HCS). $\boldsymbol{d}_{\text{cam-led}}$ is the vector from the camera principle point to the center of the LED. Note that the measured normal vectors contain uncertainties from RTK positioning, the kinematic model of the heliostat, and the reflex detection, i.e., everything that influences the start and end position of the normal vector $\boldsymbol{n}_{\text{meas}}$.

The *measured* normal vectors obtained by Eqs. (1) and (2) are then compared to the *expected* normal vectors (see Fig. 4). The expected normal vectors are calculated at all sampling point positions using the fixed kinematic model, the reference surface (by design or measured), and our best guess for the tracking angles (e.g., provided by the operator). Note that the typically limited knowledge about the kinematic model and the reference surface leads to errors in the expected normal vectors. A discussion of how the uncertainties of measured and expected normal vectors affect the result follows in the "Results and Discussion" section.

The resulting angular differences between measured and expected normal vectors can be represented as projections into the concentrator's y–z and x–z planes (rotation around x- and y-axis, respectively). The mean of the distribution of differences for y–z and x–z planes is typically not zero, meaning that the expected heliostat orientation differs from the real one. The expected tracking angles of the heliostat model are then adjusted by the value of the mean, effectively centering the angular difference distributions around zero (Fig. 5).

With this improved *expected* heliostat orientation, the normal vectors are updated and this iterative process is repeated. After usually only two iterations the changes are negligible. In the next step, a generalized extreme studentized deviate test is applied to determine outliers, and the iterative procedure is done a last time. Eventually, the final heliostat orientation is obtained. Note that this orientation corresponds to the optical axis of the heliostat relevant for operation, similar to the one measured by the conventional camera-target method. The required amount of sampled positions on the mirror surface for a robust and reliable estimation of the heliostat orientation depends strongly on the distribution of the angular differences of the heliostat mirror surface.

This calculation is done for all heliostats in the cluster, for all clusters, and for all calibration points, yielding the information to fully calibrate an entire heliostat field.

Results and Discussion

In a test campaign at the DLR solar tower plant in Jülich, the orientations of about 500 heliostats were measured. In this section, the measurement results for five of those heliostats are compared to reference data. We carry out an uncertainty analysis and demonstrate the agreement of measurement results and reference data up to the derived uncertainty. The reference data used are reference orientation vectors representing the optical axes of heliostats which are provided directly by the deflectometry-based QDec-H system [7].

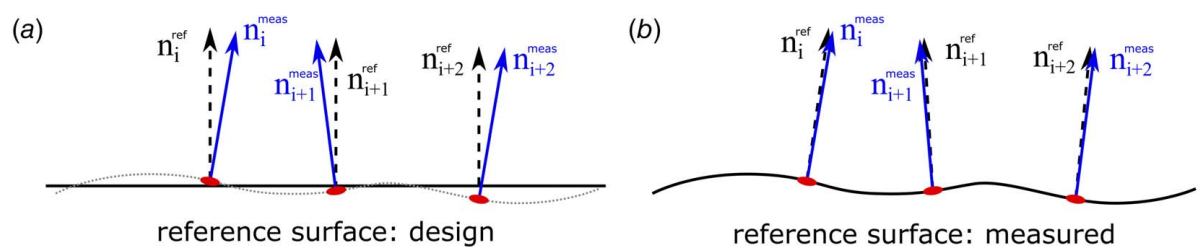

Fig. 4 Illustration of measured normal vectors (solid arrows) for various sampling points (oval shapes) on a mirror surface with slope deviations. (*a*) The dashed arrows indicate the expected normal vectors at the sampling positions perpendicular to the (flat) design surface (solid line). The design surface is used as a reference if no information about the slope deviations is available. (*b*) Considering the slope deviations (e.g., measured by the QDec-H method), small differences between the local vector pairs still remain due to other uncertainties in the heliostat kinematic model, our method (from RTK, reflex detection, etc.), or in the slope deviation measurement.

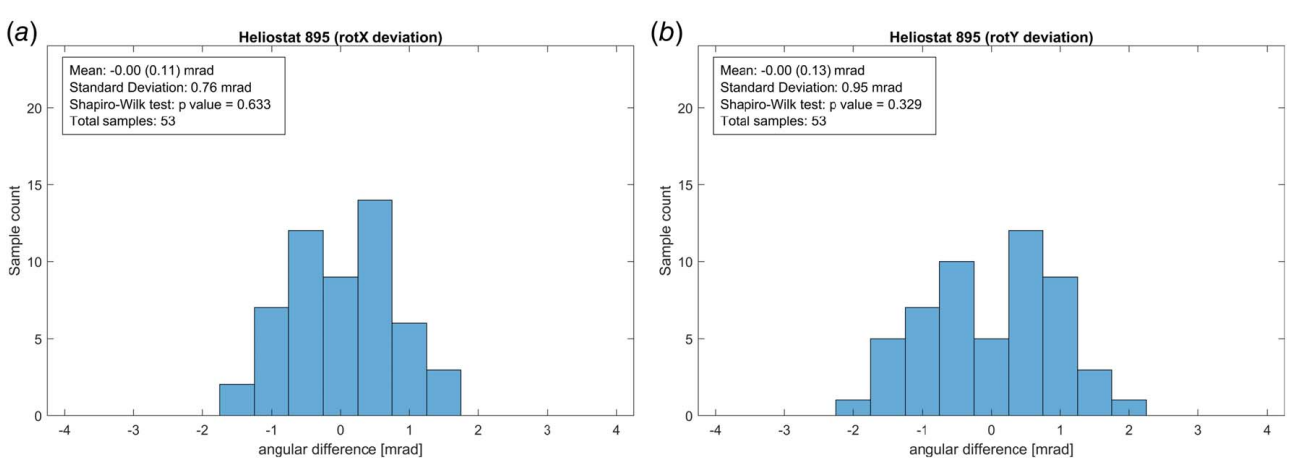

Fig. 5 Data of heliostat with ID 895 show the centered distributions of angular differences between expected (assuming an *ideal* mirror surface) and measured normal vectors for *y*–*z* plane (*a*) and *x*–*z* plane (*b*) in mrad. The data have a standard deviation of about 1 mrad dominated by surface deviations on the heliostat mirrors. Assuming a normal distribution, we obtain a standard deviation on the mean of 0.11 and 0.13 mrad for the two components, respectively.

Downloaded from http://asmedigitalcollection.asme.org/solarenergyengineering/article-pdf/146/6/061005/7354605/sol_146_6_061005.pdf by DLR Deutsches Zentrum F Luft-U Raumfahrt Ev user on 04 November 2024

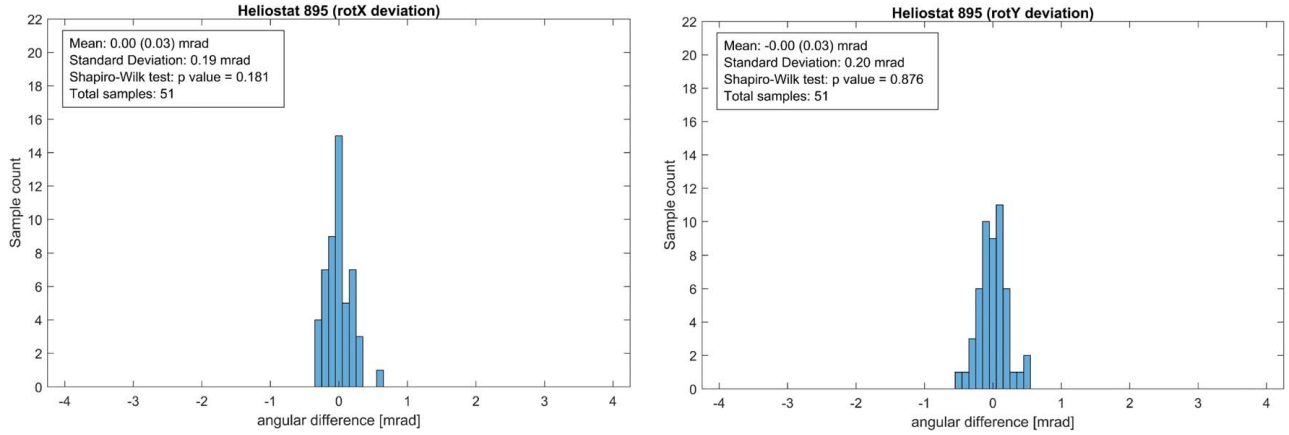

Fig. 6 Data of heliostat with ID 895 show the centered distributions of angular differences between expected (using the *premeasured* mirror surface from the QDec-H system) and measured normal vectors projected into *y–z* and *x–z* planes in mrad. The data have a standard deviation of about 0.2 mrad. This is significantly smaller than in Fig. 5, as uncertainties in the slope deviations on the heliostat mirrors are removed.

Note that the alternative approach of using the camera-target method to create reference data seems obvious but is disadvantageous, since the conversion of the measured beam profile and its position into the optical axis of the heliostat leads to additional uncertainties.

In addition to a precise (<0.1 mrad) heliostat orientation reference, the QDec-H method yields surface slope deviation maps with a precision of <0.1 mrad. Using these reference slope deviation maps allows us to exclude the uncertainty due to slope deviations from our measurement method, resulting in a reduced standard deviation of 0.2 mrad (see Fig. 6), compared to up to 1 mrad when surface slope deviation maps are not considered, as shown in Fig. 5. Given the QDec-H reference data, these surface deviations are expected to have a standard deviation of about 0.8 mrad, which agrees with our observation.

As the final heliostat orientation is derived from the angular difference distribution mean, its accuracy can be estimated from the *standard deviation of the mean estimator*.[4] In the case of normally distributed data, this quantity is given by $\sigma_{\text{mean}} = \sigma_{\text{ad}}/\sqrt{\#_{\text{samples}}}$, where σ_{ad} denotes the standard deviation of the angular difference distribution. However, this is not necessarily the case for each measured heliostat since facet canting effects or systematic surface deviations will disturb the normal distribution. Whether the assumption of a normal distribution is reasonable is decided using the Shapiro–Wilk test with a threshold of 0.05 for the resulting p-value. Datasets with a p-value larger than 0.05 are therefore considered to sample a normal distribution. For those datasets, we obtain a good value for σ_{mean} using the formula described above. If the p-value is smaller than 0.05, the normal distribution assumption has to be discarded and the calculation of the standard deviation of the mean cannot be done in the same way. Nevertheless, the order of magnitude of those values is considered to be valid.

Note that the mean standard deviation only accounts for uncertainties reflected in the width of the angular difference distribution, while additional "hidden" uncertainties $\sigma_{\text{sys},i}$ due to systematic shifts of this distribution have to be considered separately. Assuming statistical independence for the error sources, the overall uncertainty of the presented method is given as $\sigma_{\text{tot}} = \sqrt{\sigma_{\text{mean}}^2 + \Sigma_i \sigma_{\text{sys},i}^2}$. Table 1 lists potential error sources and the effect through which each error source affects the measurement uncertainty.

[4]Note that the standard deviation of the mean estimator is not the standard deviation of the distribution. The latter corresponds to the accuracy of the individual sampling points.

As the angular difference distribution compares *measured* with *expected* normal vectors, broadening or shifting in this distribution may occur due to errors in both quantities:

The *measured* normal vectors can be falsely computed because of inaccurate assumptions of camera position and/or reflex position. On the "drone side," the uncertainty of the camera position $\boldsymbol{p}_{\text{cam}}$ is determined by the accuracy of the RTK positioning, as discussed in Appendix A. While relative RTK errors of zero-mean only increase the standard deviation (i.e., broadening), an absolute RTK error leads to a systematic shift in all vectors and hence in their angles. However, we mitigate this effect by feature matching for each image. The measured normal vector is also subject to inaccuracies "on the heliostat side," i.e., in the reflex position in the global coordinate system (GCS). For the reflex detection (x_{CCS},y_{CCS}), we assume a zero-mean error, broadening but not shifting the angular difference distribution. An error in the heliostat position $\boldsymbol{p}_{\text{helio}}$, however, leads to a systematic shift in all measured normal vectors. Depending on the heliostat kinematics used in the field, an inaccurate fixed kinematic model $\mathbf{K}_{\text{helio}}$ can result in rotational and translational errors for the assumed reflex positions in the GCS, leading to both broadening and shifting.

On the other hand, the *expected* normal vectors can be subject to inaccuracies in the assumed mirror surface: While a zero-mean error distribution for the assumed mirror surface only results in broadening, a systematic error potentially impairs the method's accuracy through shifting: as an example, a falsely canted mirror facet would lead to a shift of all expected normal vectors on this facet. If the sampling distribution happened to cover only this facet, the heliostat orientation would be fitted to a falsely canted facet. To avoid this effect, a symmetric sampling point distribution should be aimed for. Such shifts are then detectable in the resulting angular difference distribution. Based on this, the operator can decide how to define the optical axis of a heliostat, depending on the specific application.

The uncertainties of the mean and the p-value for the corresponding distribution for all five heliostats are summarized in Table 2. From these numbers, we derive a conservative mean estimation uncertainty of $\sigma_{\text{mean}} = 0.2$ mrad for measurements using the ideal mirror surface. This uncertainty is reduced to below 0.1 mrad when using the precise surface maps from QDec-H.

Additionally, we consider the uncertainty due to systematic shifts based on the following considerations: for large distances d between camera and heliostats, the standard deviations $\sigma_{\text{x},i}$ of assumed camera position and reflex position translate to angle uncertainties according to $\sigma_{\text{sys},i} = \sigma_{\text{x},i}/d$. Assuming no absolute error in the RTK positioning, uncertainties of 10 mm for $\boldsymbol{p}_{\text{helio}}$, 30 mm for shifts due to errors in $\mathbf{K}_{\text{helio}}$, and no systematic errors in the

Downloaded from http://asmedigitalcollection.asme.org/solarenergyengineering/article-pdf/146/6/061005/7354605/sol_146_6_061005.pdf by DLR Deutsches Zentrum F Luft-U Raumfahrt Ev user on 04 November 2024

Table 1 List of the considered error sources which lead to shifting or broadening of the angular difference distribution

Error source	Broadening σ_{mean}	Shifting $\sigma_{sys,i}$
RTK relative $\boldsymbol{p}_{cam}$	x	–
RTK absolute $\boldsymbol{p}_{cam}$	–	(x)
Reflex detection (x_{CCS},y_{CCS})	x	–
Heliostat position $\boldsymbol{p}_{helio}$	–	x
Heliostat kinematics $\mathbf{K}_{helio}$	x	x
Assumed mirror surface – zero-mean errors	x	–
Assumed mirror surface – systematic errors (e.g., canting)	–	For nonsymmetric sampling point distributions

Uncertainties due to broadening are extracted from the statistics of the data. For shifts, the potential uncertainty has to be determined and added quadratically to the uncertainty of the mean estimator. The individual error sources are discussed in the text.

Table 2 Mean estimation uncertainty results regarding rotation around *x*- and *y*-axis of the examined heliostats for an evaluation using the ideal mirror surface and the measured mirror surface

Heliostat ID		Using ideal surface		Using measured surface	
		σ_{mean} (mrad)	*p*-value	σ_{mean} (mrad)	*p*-value
894	rotX	0.14	0.31	0.02	0.38
	rotY	0.19	0.21	0.03	0.73
895	rotX	0.11	0.63	0.03	0.18
	rotY	0.13	0.33	0.03	0.88
913	rotX	0.11	0.12	0.02	0.61
	rotY	0.08	0.94	0.03	0.01
917	rotX	0.10	0.26	0.03	0.93
	rotY	0.13	0.78	0.04	0.49
1089	rotX	0.13	0.22	0.02	0.20
	rotY	0.15	0.09	0.03	0.05

The *p*-values stem from the Shapiro–Wilk test. Numbers above 0.05 support the hypothesis of a normal distribution of the data, indicating that the given uncertainties are calculated correctly. Uncertainties where $p < 0.05$ have to be treated with care, but the order of magnitude is assumed to be correct.

Table 3 Differences of the orientation measurement for rotX and rotY when compared against reference data obtained from QDec-H

Heliostat ID		Offset to reference (mrad)	
		Using ideal surface	Using measured surface
894	rotX	−0.14	−0.10
	rotY	0.00	0.01
895	rotX	0.01	0.05
	rotY	−0.05	0.07
913	rotX	0.18	0.04
	rotY	0.54	0.55
917	rotX	0.19	0.00
	rotY	0.15	0.20
1089	rotX	0.34	0.31
	rotY	−0.07	0.04

The uncertainty of the reference data is given as <0.1 mrad.

mirror surface, the additional systematic uncertainty amounts to $\sigma_{sys} = 0.2$ mrad at a distance of 150 m.

This gives us a conservative estimate for the overall measurement uncertainty of $\sigma_{tot} = 0.3$ mrad using an ideal mirror surface. Note that the numerical values in this computation may change depending on the available prior knowledge on heliostat positions, kinematic model, and surface slope deviations.

The offset of our final orientation results to the QDec-H reference data is shown in Table 3. Here, we find very good agreement between our measurement and QDec-H data, considering the uncertainties as described above and the ones from the reference of <0.1 mrad. The complete sampling data for each heliostat are presented in Appendix B.

Conclusion

We present a fast and accurate airborne calibration method for heliostats, prepared for commercial application, and demonstrate its accuracy on the tracking offset to be better than 0.3 mrad, which qualifies this method as a so-called fine-calibration method. The method only requires an LED and a camera fitted to a drone. Since this method can be applied to bigger groups of heliostats at once, the projected calibration time of a commercial plant can be reduced to a few weeks including data acquisition and evaluation instead of many months or even years using the state-of-the-art methodology. This significantly shortens the commissioning time and performance guarantee period of new plants, reducing their costs and increasing their viability. Compared to competitive alternative techniques, our method does not require any other infrastructure apart from the heliostats installed at the plant and can therefore be applied early on during commissioning. Furthermore, it works independently of the sun position and the time of the year.

Acknowledgment

Financial support from the German Federal Ministry for Economic Affairs and Climate Action (HelioPoint-II, contract 3028684) is gratefully acknowledged. We also thank our DLR colleagues Oliver Kaufhold and Felix Göhring at the solar tower in Jülich, Germany.

Conflict of Interest

There are no conflicts of interest.

Data Availability Statement

The authors attest that all data for this study are included in the article.

Nomenclature

d = distance (m)
k = kinematic parameter (various)
$\boldsymbol{d}$ = vector pointing from one position to another position (m)
$\boldsymbol{n}$ = normal vector (m)
$\boldsymbol{p}$ = position (m)
$\mathbf{K}$ = kinematic model (m)

Greek Symbols

θ = light vector angle (rad/deg)
σ = standard deviation (rad/deg/m)
φ = heliostat tracking angle (rad/deg)

Subscripts

ad = angular difference
cam = camera
cam-led = from camera to LED
helio = heliostat
i = index for iteration
mean = mean/average
meas = measured
ref = reference

Downloaded from http://asmedigitalcollection.asme.org/solarenergyengineering/article-pdf/146/6/061005/7354605/sol_146_6_061005.pdf by DLR Deutsches Zentrum F Luft-U Raumfahrt Ev user on 04 November 2024

reflex = reflex
sys = systematic
tot = total

Abbreviations

CCS = concentrator coordinate system
GCS = global coordinate system
GPS = global positioning system
HCS = heliostat coordinate system
ID = identification
LED = light-emitting diode
RTK = real-time kinematics

Appendix A: Measuring Real-Time Kinematics Positioning Precision

For a precise evaluation of our method, it is essential that next to the heliostat position and kinematic model, also the drone position is well known. We use a drone equipped with real-time kinematics (RTK) to obtain an offset-corrected GPS position for each image. To measure the accuracy of our system, we performed a dome-shaped flight as illustrated in Fig. 7. For each image, we obtain the RTK data, and for comparison, we evaluate all images photogrammetrically using the commercial software AICON 3D STUDIO.

The photogrammetric evaluation yields sub-mm precise camera positions. For the evaluation, the RTK data, as well as the camera positions from AICON 3D STUDIO, are represented as point clouds. The photogrammetry data are then fitted into the RTK data to evaluate the relative precision of the latter. The results as shown in Fig. 8 indicate a standard deviation of the RTK precision for the Cartesian components of about 6–8 mm with a maximum for the z-component. The covariance of the data shows an approximate linear independence of the components. As a conservative upper limit for the standard deviation of any arbitrary component (which would be chosen according to the camera orientation of a specific image), we can use 10 mm. For typical camera-to-heliostat distances of more than 100 m, this results in an error of less than 0.1 mrad for each individual sampling point. The effect is linearly reduced for larger distances and averaged out for several sampling points as used to evaluate the heliostat orientation. We therefore conclude that the relative RTK uncertainty is negligible for this method. In contrast, a potential systematic global positioning offset (with respect to the solar field) has a direct effect on the calibration results. However, the uncertainty of such a global positioning offset can be reduced by reference markers in the field, which, e.g., can be represented by the heliostats. Due to the good relative precision, all images can be used to improve the global position, which should result in global accuracies of similar magnitude (~10 mm) as the relative accuracies.

Appendix B: Detailed Data of the Five Calibrated and Validated Heliostats

Tables 4 and 5 show the orientations of the five heliostats as measured compared to the reference values for azimuth and elevation, respectively.

For the sake of completeness, Figs. 9–13 show for each heliostat the sampling distribution and mirror surface maps, as well as the angular offsets decomposed into rotations around x- and y-axis for evaluations using ideal and measured mirror surface maps.

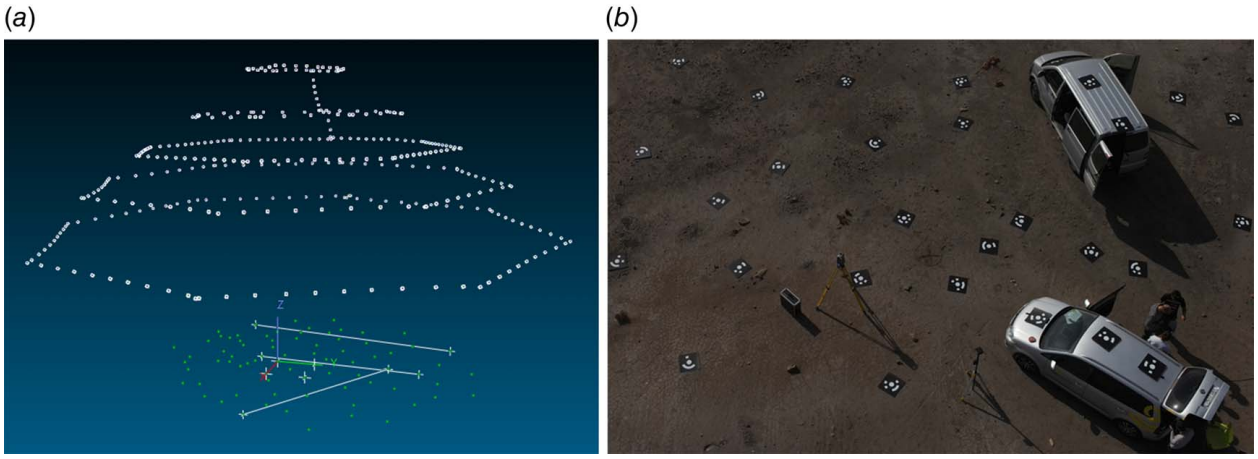

Fig. 7 (*a*) Screenshot of the Aicon evaluation showing the camera positions (bright boxes in the upper region of the image) for all images and the coded targets on the ground (darker dots in the lower region of the image). (*b*) Drone image of the measurement scene showing the coded targets on the ground.

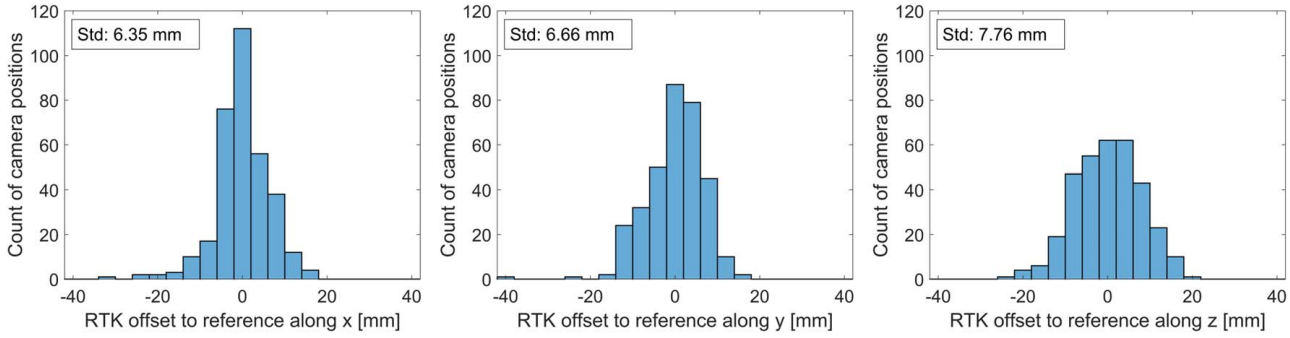

Fig. 8 Relative RTK position errors in *x*, *y*, and *z* (from left to right) in a local Cartesian coordinate system with respect to a photogrammetric evaluation, not considering global offsets

Downloaded from http://asmedigitalcollection.asme.org/solarenergyengineering/article-pdf/146/6/061005/7354605/sol_146_6_061005.pdf by DLR Deutsches Zentrum F Luft-U Raumfahrt Ev user on 04 November 2024

Table 4 Orientation as AZIMUTH angle for: (a) measurement results using ideal heliostat shape, (b) measured results using precise surface information, and (c) reference results from QDec-H measurement

	(a) "Ideal"		(b) "Meas"		
Heliostat ID	Absolute (deg)	Deviation from "Ref" (mrad)	Absolute (deg)	Deviation from "Ref" (mrad)	(c) "Ref" (deg)
894	213.080	0.02	213.080	0.03	213.081
895	214.057	0.05	214.051	0.07	214.054
913	214.738	0.53	214.736	0.56	214.768
917	215.060	0.12	215.055	0.20	215.067
1089	213.318	0.13	213.312	0.01	213.311

Table 5 Orientation as ELEVATION angle for: (a) measurement results using ideal heliostat shape, (b) measured results using precise surface information, and (c) reference results from QDec-H measurement

	(a) "Ideal"		(b) "Meas"		
Heliostat ID	Absolute (deg)	Deviation from "Ref" (mrad)	Absolute (deg)	Deviation from "Ref" (mrad)	(c) "Ref" (deg)
894	13.609	0.13	13.611	0.10	13.616
895	13.547	0.00	13.550	0.06	13.547
913	14.948	0.25	14.940	0.11	14.934
917	13.460	0.21	13.450	0.03	13.448
1089	12.363	0.33	12.362	0.31	12.345

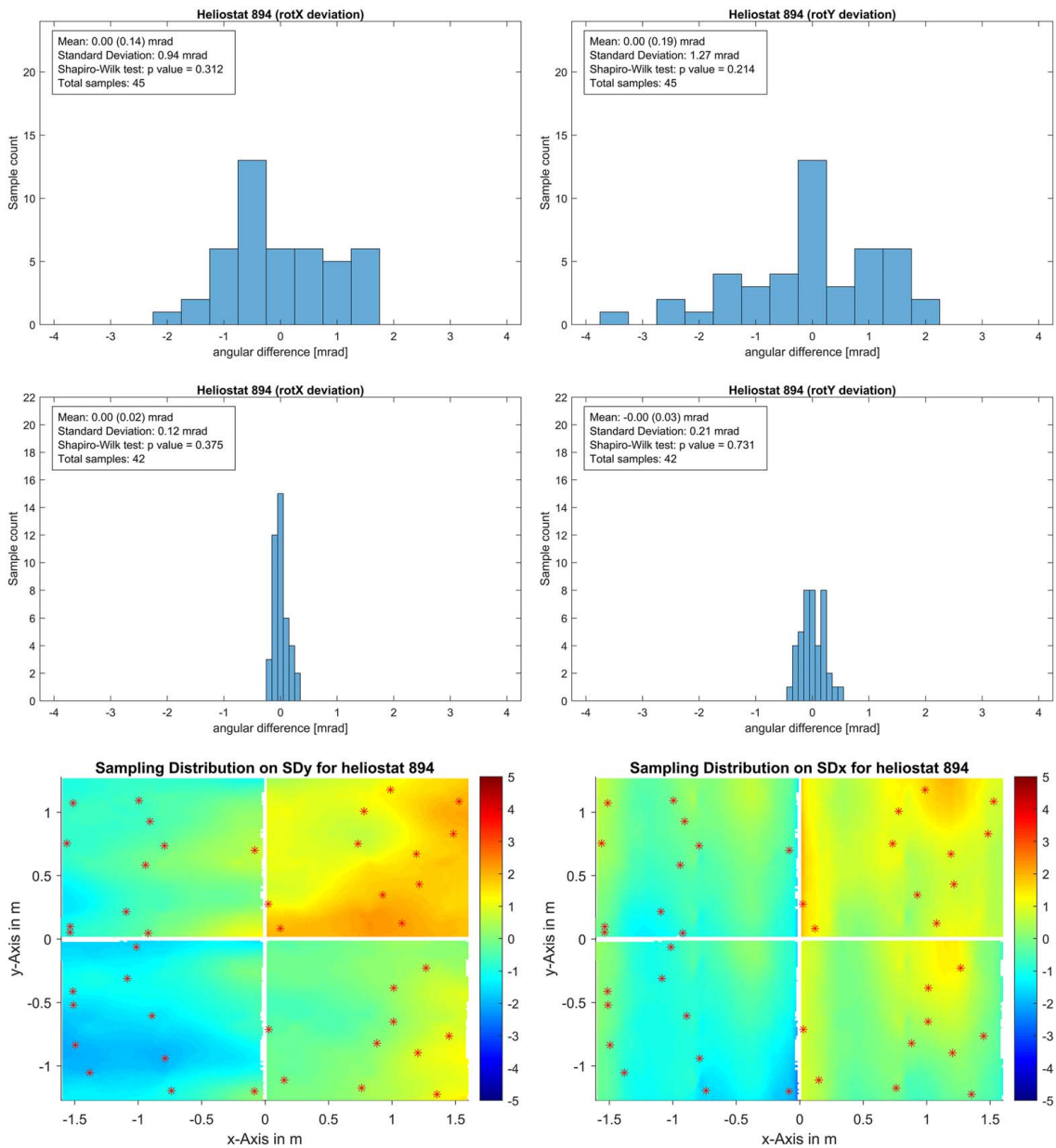

Fig. 9 Data of heliostat with ID 894. Angular differences between local normal vector pairs decomposed in rotations around *x*- (left) and *y*-axis (right). The local reference vectors are calculated using the design mirror surface (top) or the measured surface slope deviation map (center). The bottom graphs show the measured slope deviations in mrad and the positions of the sampling points (asterisks) on the heliostat mirror surface. Note that SDy and SDx refer to slope deviations along the *y*- and *x*-axis, respectively, which means SDy corresponds to rotations around the *x*-axis (rotX) and SDx to rotations around the *y*-axis (rotY)

Downloaded from http://asmedigitalcollection.asme.org/solarenergyengineering/article-pdf/146/6/061005/7354605/sol_146_6_061005.pdf by DLR Deutsches Zentrum F Luft-U Raumfahrt Ev user on 04 November 2024

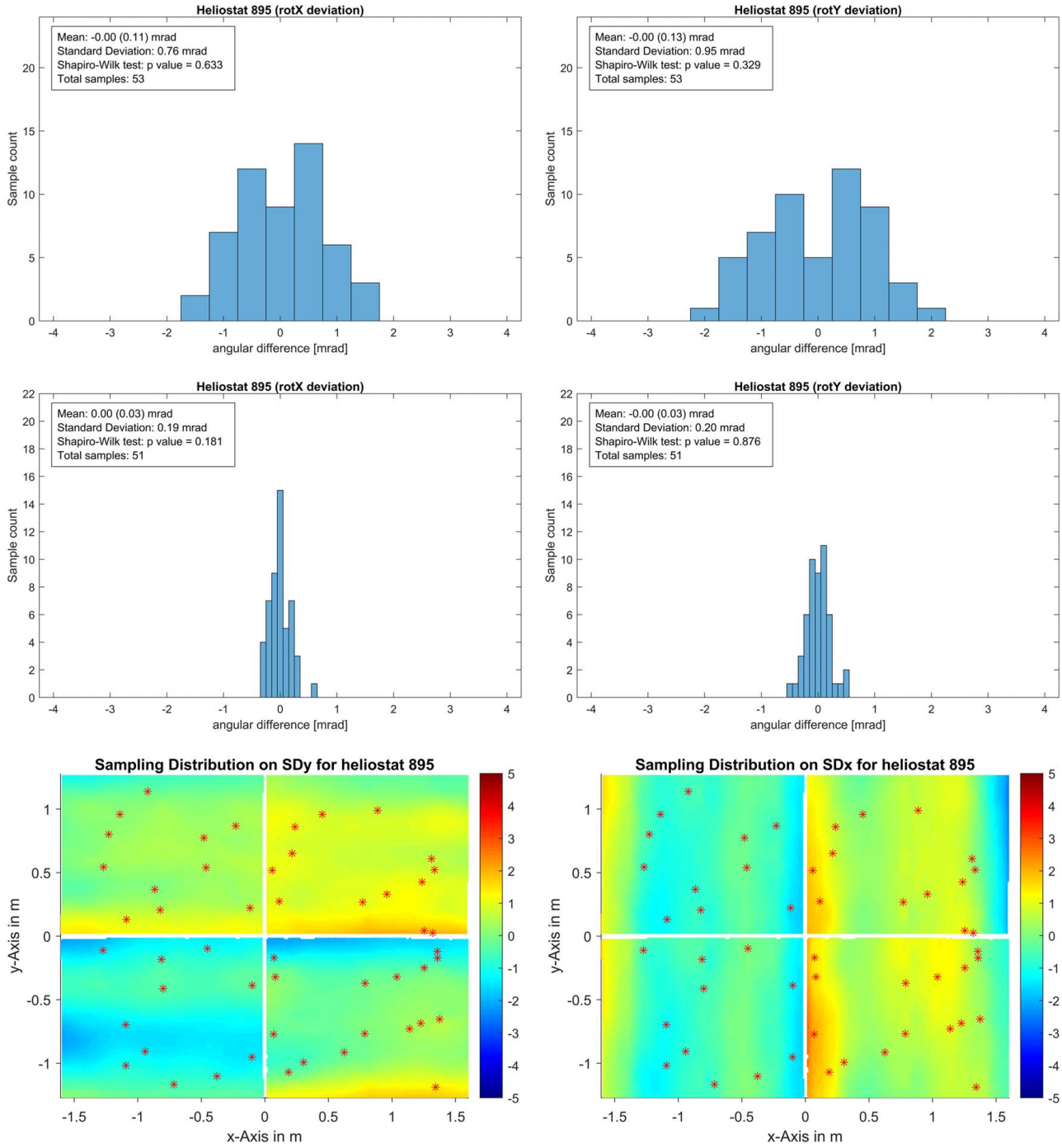

Fig. 10 Data of heliostat with ID 895. Angular differences between local normal vector pairs decomposed in rotations around *x*- (left) and *y*-axis (right). The local reference vectors are calculated using the design mirror surface (top) or the measured surface slope deviation map (center). The bottom graphs show the measured slope deviations in mrad and the positions of the sampling points (asterisks) on the heliostat mirror surface. Note that SDy and SDx refer to slope deviations along the *y* and *x*-axis, respectively, which means SDy corresponds to rotations around the *x*-axis (rotX) and SDx to rotations around the *y*-axis (rotY).

Downloaded from http://asmedigitalcollection.asme.org/solarenergyengineering/article-pdf/146/6/061005/7354605/sol_146_6_061005.pdf by DLR Deutsches Zentrum F Luft-U Raumfahrt Ev user on 04 November 2024

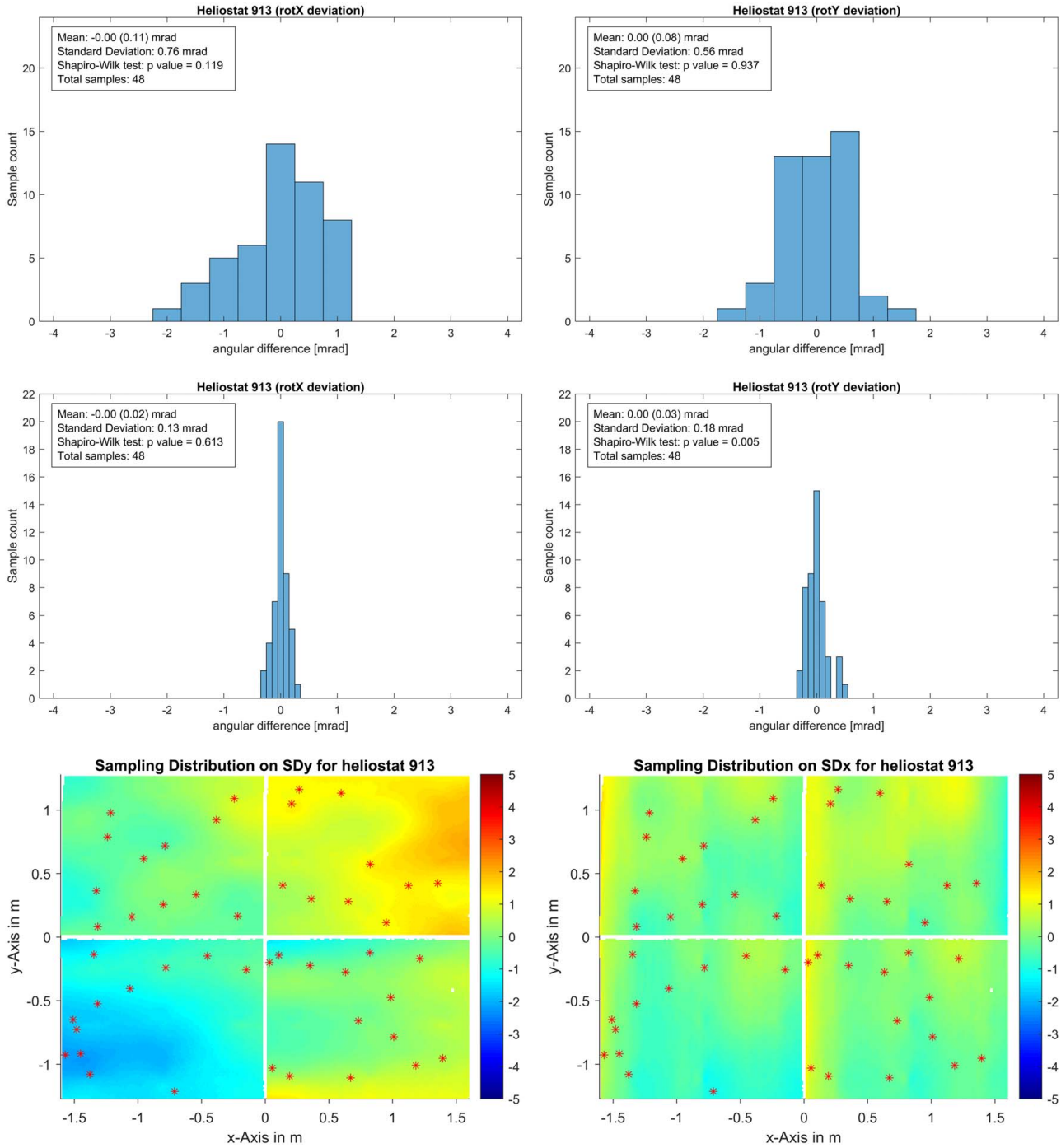

Fig. 11 Data of heliostat with ID 913. Angular differences between local normal vector pairs decomposed in rotations around *x*- (left) and *y*-axis (right). The local reference vectors are calculated using the design mirror surface (top) or the measured surface slope deviation map (center). The bottom graphs show the measured slope deviations in mrad and the positions of the sampling points (asterisks) on the heliostat mirror surface. Note that SDy and SDx refer to slope deviations along the *y*- and *x*-axis, respectively, which means SDy corresponds to rotations around the *x*-axis (rotX) and SDx to rotations around the *y*-axis (rotY).

Downloaded from http://asmedigitalcollection.asme.org/solarenergyengineering/article-pdf/146/6/061005/7354605/sol_146_6_061005.pdf by DLR Deutsches Zentrum F Luft-U Raumfahrt Ev user on 04 November 2024

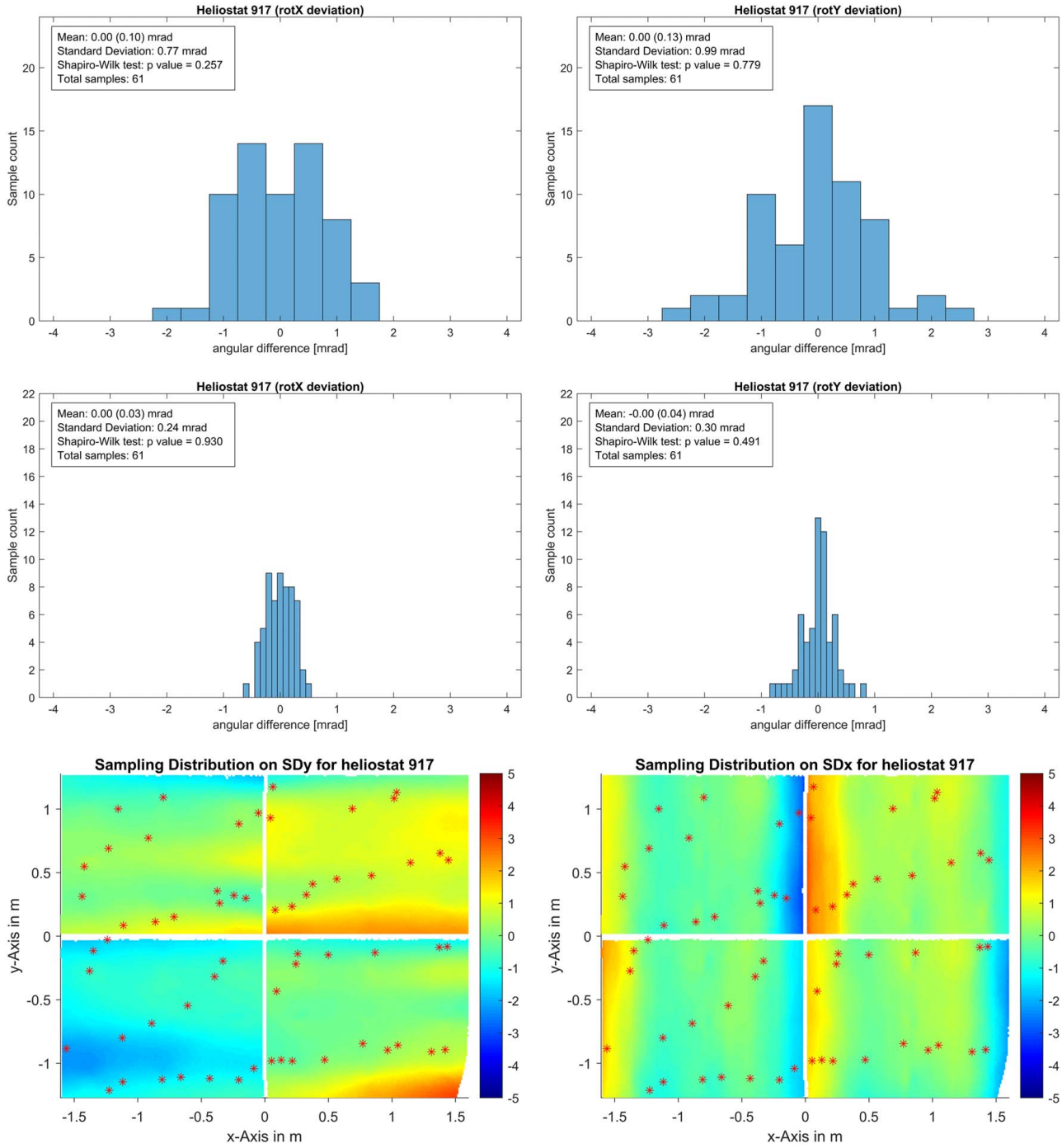

Fig. 12 Data of heliostat with ID 917. Angular differences between local normal vector pairs decomposed in rotations around *x*- (left) and *y*-axis (right). The local reference vectors are calculated using the design mirror surface (top) or the measured surface slope deviation map (center). The bottom graphs show the measured slope deviations in mrad and the positions of the sampling points (asterisks) on the heliostat mirror surface. Note that SDy and SDx refer to slope deviations along the *y*- and *x*-axis, respectively, which means SDy corresponds to rotations around the *x*-axis (rotX) and SDx to rotations around the *y*-axis (rotY).

Downloaded from http://asmedigitalcollection.asme.org/solarenergyengineering/article-pdf/146/6/061005/7354605/sol_146_6_061005.pdf by DLR Deutsches Zentrum F Luft-U Raumfahrt Ev user on 04 November 2024

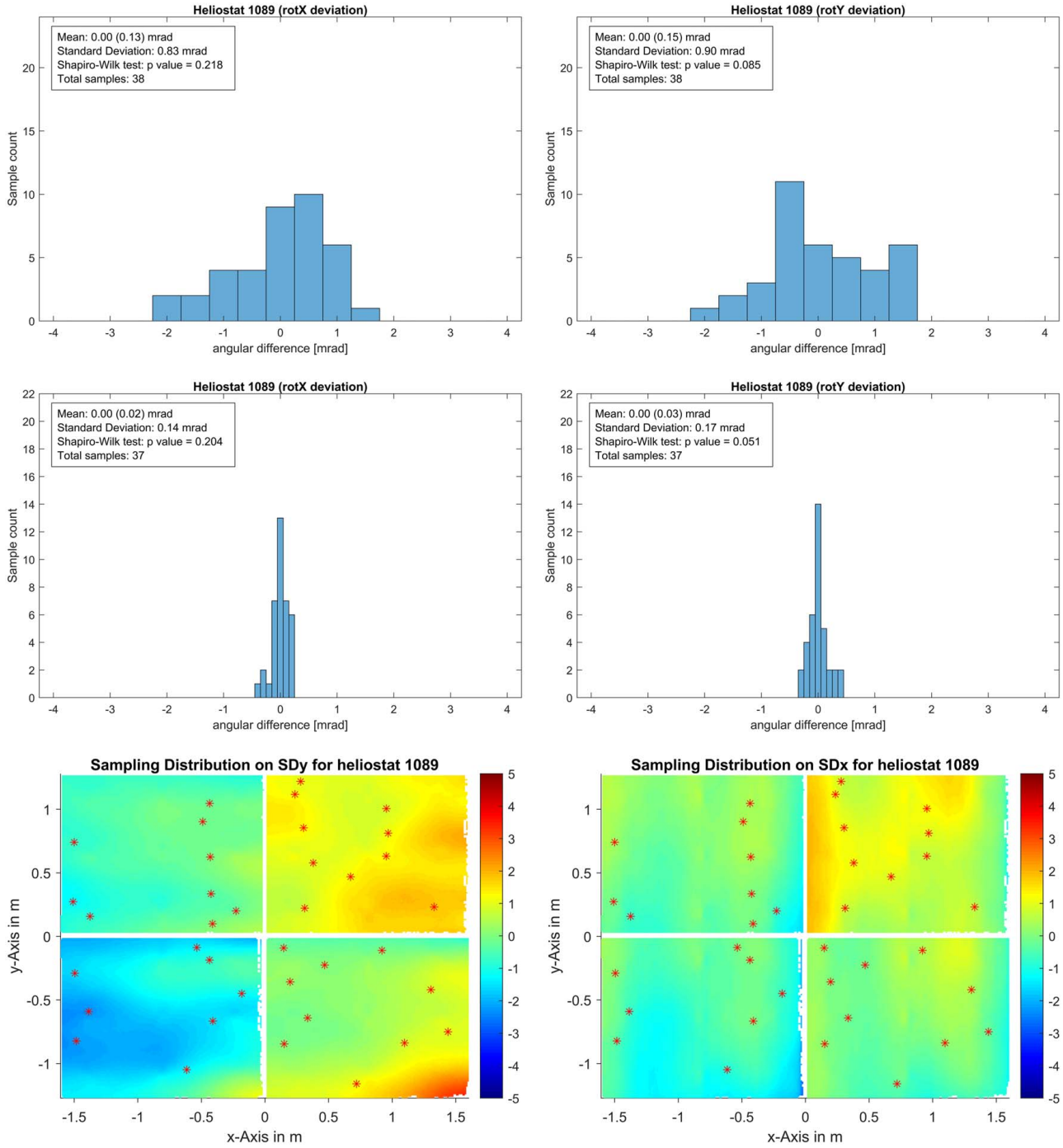

Fig. 13 Data of heliostat with ID 1089. Angular differences between local normal vector pairs decomposed in rotations around *x*- (left) and *y*-axis (right). The local reference vectors are calculated using the design mirror surface (top) or the measured surface slope deviations map (center). The bottom graphs show the measured slope deviations in mrad and the positions of the sampling points (asterisks) on the heliostat mirror surface. Note that SDy and SDx refer to slope deviations along the *y*- and *x*-axis, respectively, which means SDy corresponds to rotations around the *x*-axis (rotX) and SDx to rotations around the *y*-axis (rotY).

References

[1] Sattler, J., Röger, M., Schwarzbözl, P., Buck, R., Macke, A., Raeder, C., and Göttsche, J., 2020, "Review of Heliostat Calibration and Tracking Control Methods," Sol. Energy, **207**, pp. 110–132.

[2] Stone, K. W., "Automatic Heliostat Track Alignment Method," U.S. Patent No. 4,564,275. https://patents.google.com/patent/US4564275A.

[3] Zhu, G., Augustine, C., Mitchell, R., Muller, M., Kurup, P., Zolan, A., Yellapantula, S., et al., 2022, "Roadmap to Advance Heliostat Technologies for Concentrating Solar-Thermal Power," Technical Report No. NREL/TP-5700-83041.

[4] Göhring, F., Hilgert, C., Ulmer, S., Prahl, C., and Röger, M., "Verfahren zur Vermessung von Heliostaten," German Patent No. 102015217086. https://patents.google.com/patent/DE102015217086A1.

[5] Jessen, W., Röger, M., Prahl, C., and Pitz-Paal, R., 2022, "A Two-Stage Method for Measuring the Heliostat Offset," Proceedings of the 26th International Conference on Concentrating Solar Power and Chemical Energy Systems (SolarPACES), Freiburg, Germany, Sept. 28–Oct. 2, p. 070005.

[6] Mitchell, R. A., and Zhu, G., 2020, "A Non-Intrusive Optical (NIO) Approach to Characterize Heliostats in Utility-Scale Power Tower Plants: Methodology and In-Situ Validation," Sol. Energy, **209**, pp. 431–445.

[7] Schwarzbözl, P., Rong, A., Macke, A., Säck, J.-P., and Ulmer, S., 2016, "An Automated Model-Based Aim Point Distribution System for Solar Towers," Proceedings of the 21st International Conference on Concentrating Solar Power and Chemical Energy Systems (SolarPACES), Cape Town, South Africa, Oct. 13–16, p. 020023.

Downloaded from http://asmedigitalcollection.asme.org/solarenergyengineering/article-pdf/146/6/061005/7354605/sol_146_6_061005.pdf by DLR Deutsches Zentrum F Luft-U Raumfahrt Ev user on 04 November 2024